# Calibration and Application of GISSMO and *MAT_258 for Simulations Using Large Shell Elements

Joakim Johnsen[1], Jens Kristian Holmen[1], Gaute Gruben[4], David Morin[2,3], Magnus Langseth[2,3]
[1]*Enodo AS, Trondheim, Norway*
[2]*Structural Impact Laboratory (SIMLab), Department of Structural Engineering, Norwegian University of Science and Technology (NTNU), Trondheim, Norway*
[3]*Centre for Advanced Structural Analysis (SFI CASA), NTNU, Trondheim, Norway*
[4]*SINTEF Industry, Materials and Nanotechnology, Trondheim, Norway*

## Abstract

*For many industrial applications finite element (FE) models are becoming increasingly large, making shell elements a necessary tool to maintain a reasonable computational time. Shell elements describe a plane stress state and phenomena like local necking and failure under bending must be appropriately dealt with. Thickness-to-length ratios larger than two are not uncommon for shell elements. This is often larger than the elements used for material model calibration and can sometimes lead to challenges in describing the geometry and the stress state. In this study, we evaluate the accuracy of *MAT_258 and a standard GISSMO calibration. The material and component tests are made of Docol 1400M. Results from *MAT_258 and GISSMO are compared to several component tests spanning a wide range of stress states.*

## 1 Introduction

Shell elements are the typical choice when modelling mid- to large-scale structural problems in the industry. These elements work well when dealing with elastic-plastic material behavior and can usually be applied with confidence. On the other hand, when damage and failure occur, predicting accurate behavior becomes more challenging due to strain localization or local necking. Necking is challenging to describe with shell elements because (1) the elements are typically larger than the localization zone and (2) because shell elements are limited to plane stress conditions. When a neck forms, strain localization turns into a triaxiality-driven problem, meaning that all six stress and strain components are essential to describe the material behavior correctly.

In this study we compare the well-known GISSMO failure model [1] with the newly proposed through-thickness damage regularization model (TTR) [2,6] available as *MAT_258 (*MAT_NON_QUADRATIC_FAILURE) in LS-DYNA® applied to Docol 1400M high-strength steel. After calibration, both failure models are validated by three-point bending experiments on purpose-made hat profiles.

## 2 Experiments

The Docol 1400M steel material was delivered in 1.0 mm thick sheets. Uniaxial tension (UT), plane strain tension (PST), in-plane simple shear (ISS) and equi-biaxial tension Nakajima tests (NK) were performed to cover a wide range of stress states before fracture [4]. All experiments were conducted at room temperature under quasi-static loading rates. To facilitate digital image correlation (DIC), all experiments were monitored by digital cameras. Two-dimensional (2D) DIC was used in all experiments except the Nakajima tests, where two cameras were used to enable three-dimensional (3D) DIC. For a detailed description of the experimental program, the interested reader is referred to Gaute et al. [4].

## 2.1 Uniaxial tension

The specimen geometry used in the UT tests is shown in Figure 1.

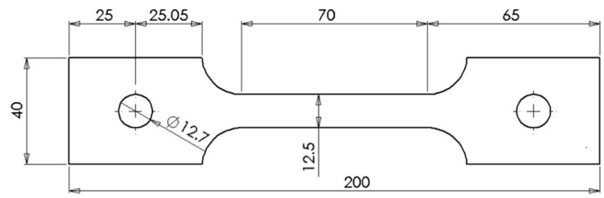


Figure 1: Geometry of the UT specimens.

Three repetitions were conducted in a hydraulic testing machine (Zwick/Roell) at a constant crosshead velocity of 4 mm/min, equating to a nominal strain rate of $1 \cdot 10^{-3}\ \mathrm{s}^{-1}$. A virtual extensometer with a length of 60 mm was used to calculate the engineering strain $e = (L - L_0)/L_0$, where $L$ and $L_0$ are the current and initial extensometer length, respectively. The engineering stress was found as $\sigma = F/A_0$, where $F$ is the force measured by the testing machine and $A_0$ is the initial cross-section area. The engineering stress-strain curves for the UT tests are given in Figure 2.

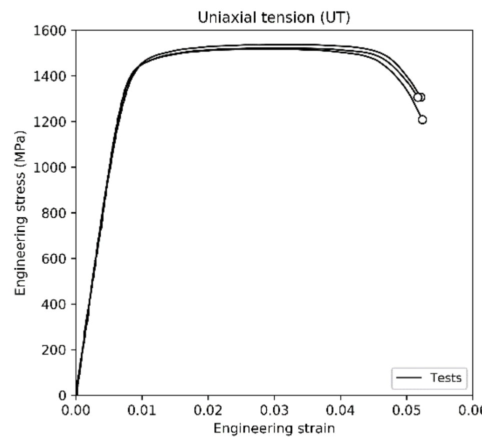


Figure 2: Engineering stress-strain curve from UT tests.

## 2.2 Plane strain tension

Figure 3 shows the specimen geometry used in the PST experiments Three PST experiments were conducted in an Instron 5900 hydraulic testing machine at a constant crosshead velocity of 0.9 mm/min, yielding an initial nominal strain rate of $1.0 \cdot 10^{-3}\ \mathrm{s}^{-1}$ [4]. A virtual extensometer with an initial length of 18.5 mm was used to calculate the engineering strain, while the normalized force was found from the load cell and the cross-section area at the center of the gauge. The engineering stress-strain curves obtained from experiments are given in Figure 4.

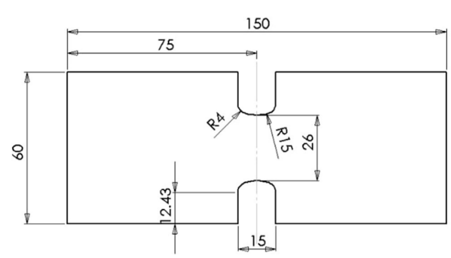


Figure 3: Specimen geometry for plane strain tests.

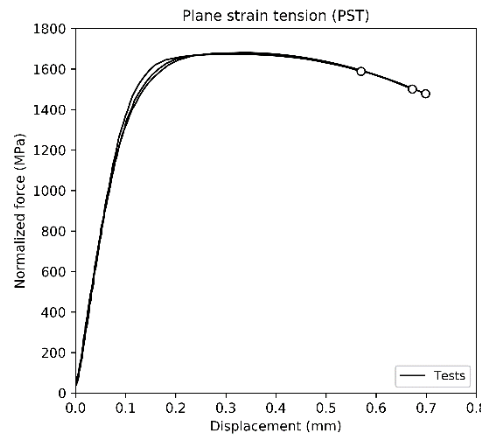


Figure 4: Normalized force-strain curves from PST experiments.

## 2.3 In-plane simple shear

The same Zwick/Roell hydraulic machine as in the UT experiments were used for the in-plane simple shear tests. A constant cross-head velocity of 0.3 mm/min was used, translating to an initial nominal shear strain rate of $1.0 \cdot 10^{-3}\ \mathrm{s}^{-1}$ based on the nominal width of the gauge section of the specimen shown in Figure 5a.

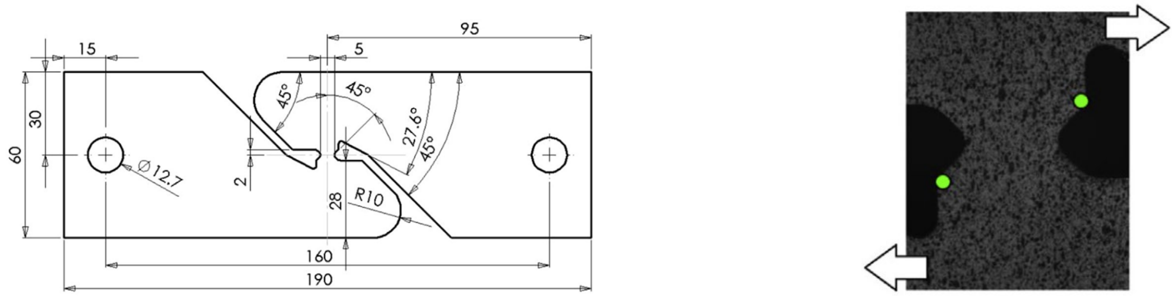


(a) (b)

Figure 5: (a) Geometry of the specimens used in the ISS tests and (b) the points used for the virtual extensometer.

A virtual extensometer was applied to the diagonal of the gauge section as illustrated in Figure 5b and was used to calculate the displacement, the normalized force was calculated as $F/A_0$, where $F$ is the force found from the load cell and $A_0$ is the minimum initial cross-section in the gauge. Figure 6 shows the resulting normalized force vs. displacement curves for the three repetitions.

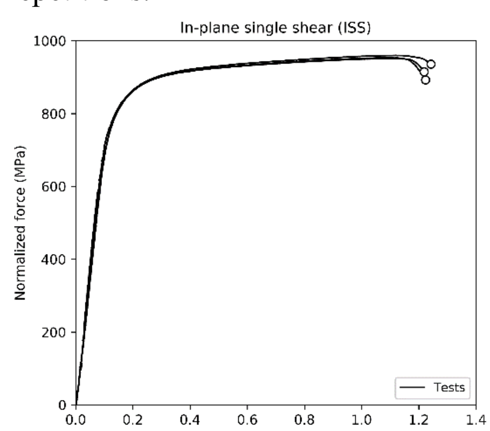


Figure 6: Normalized force vs. displacement from the ISS experiments.

## 2.4 Nakajima tests

The Nakajima (NK) test-setup [7] is shown in Figure 7. Four repetitions were performed in a Zwick/Roell BUP 600 test machine, where a punch with a constant velocity of 0.3 mm/s was used to load the specimens [4].

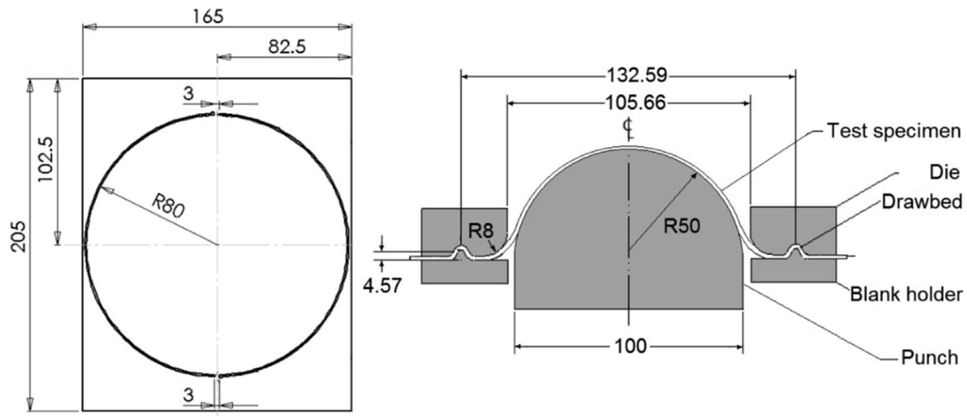


Figure 7: Dimensions of the equi-biaxial Nakajima specimen and details showing the experimental set-up.

A total clamping force of 200 kN was applied to hold the specimen in place during the test. To reduce friction, grease was applied to the punch in addition placing a 0.1 mm thick teflon sheet between the punch and the specimen [4]. To capture the out-of-plane deformation 3D DIC was used. Figure 8 shows the force vs. displacement curves obtained from the experiments.

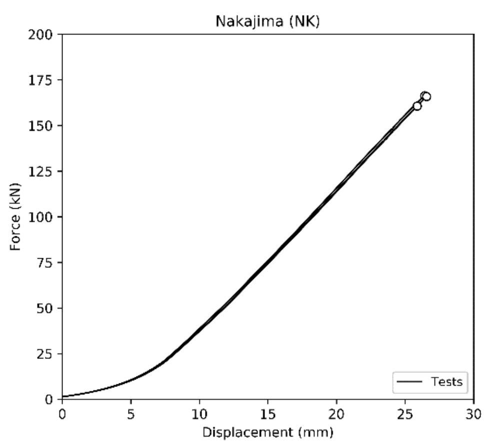


Figure 8: Force vs. displacement curves from the NK tests.

# 3 Material modelling

## 3.1 *MAT_NON_QUADRATIC_FAILURE/*MAT_258

The *MAT_NON_QUADRATIC_FAILURE/*MAT_258 material model was developed by Costas et al. [2], who proposed and validated a damage regularization model for shell elements used in large-scale simulations.

The yield function is given as

$$f = \sigma_{\text{eq}} - \left(\sigma_0 + R(p)\right) \tag{1}$$

where $\sigma_{\text{eq}}$ is the Hershey-Hosford equivalent stress defined as

$$\sigma_{\text{eq}} = \left[\frac{1}{2}\left(|\sigma_1 - \sigma_2|^a + |\sigma_2 - \sigma_3|^a + |\sigma_1 - \sigma_3|^a\right)\right]^{\frac{1}{a}} \tag{2}$$

where $\sigma_1, \sigma_2, \sigma_3$ are the major, intermediate and minor principal stresses and $a$ is the exponent controlling the curvature of the yield surface. If $a = 2$ or $a = 4$ the Hershey-Hosford equivalent stress is equal to the von Mises equivalent stress, and if $a = 1$ or $a \to \infty$ it is equal to the Tresca equivalent stress. As is customary for steel, the exponent $a = 6$, see Figure 9.

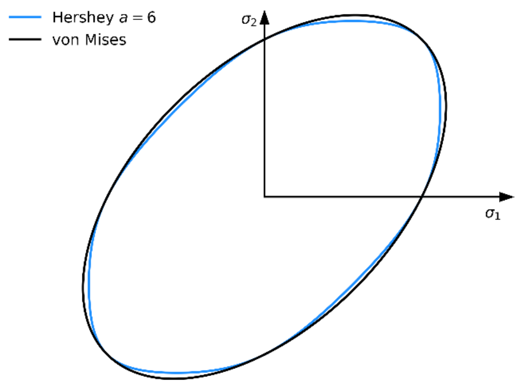


Figure 9: Hershey-Hosford yield locus with an exponent of $a = 6$ vs. the von Mises yield locus.

Furthermore, $\sigma_0$ is the initial yield stress and $R(p)$ is the work hardening defined by a three-term Voce expression

$$R(p) = \sum_{i=1}^{3} Q_i \left[1 - \exp\left(-\frac{\theta_i}{Q_i} p\right)\right] \tag{3}$$

where $Q_i$ determines the saturation levels, $\theta_i$ controls the hardening rate and $p$ is the equivalent plastic strain found by associated flow. Strain rate sensitivity is not included in this study, but is available in *MAT_258 through the constitutive relation

$$\dot{p} = \begin{cases} 0, & \text{if } f \leq 0 \\ \dot{p}_0 \left[1 - \left(\dfrac{\sigma_{\text{eq}}}{\sigma_0 + R(p)}\right)^{\frac{1}{C_\sigma}}\right], & \text{if } f > 0 \end{cases} \tag{4}$$

where $\dot{p}_0$ is a reference equivalent plastic strain rate and $C_\sigma$ is a strain rate sensitivity parameter. The viscoplastic equivalent stress then reads

$$\sigma_{\mathrm{eq}} = \left(\sigma_0 + R(p)\right)\left(1 + \frac{\dot{p}}{\dot{p}_0}\right)^{C_\sigma} \tag{5}$$

Note that strain rate sensitivity is not included in our simulations, i.e. $C_\sigma = 0$. The extended Cockcroft-Latham (ECL) failure criterion [5] is available, viz.

$$\dot{D} = \frac{\sigma_{\mathrm{eq}}}{W_{\mathrm{c}}}\left\langle \phi \frac{\sigma_1}{\sigma_{\mathrm{eq}}} + (1-\phi)\left(\frac{\sigma_1 - \sigma_3}{\sigma_{\mathrm{eq}}}\right)\right\rangle^{\gamma} \dot{p} \ \wedge \ D \leq 1 \tag{6}$$

where $\langle x \rangle = 0.5(|x| + x)$, $W_c$ is the Cockcroft-Latham failure parameter, $\phi$ and $\gamma$ are parameters controlling the shape of the failure surface. Failure, in the form of element erosion, occurs when the damage parameter $D \geq 1$. Setting $\phi = \gamma = 1$ reduces the failure criterion to the original Cockcroft-Latham failure criterion.

To regularize the failure criterion, Costas et al. [2,6] proposed to distinguish between bending and membrane loading. First, a bending parameter was introduced as

$$\Omega = \frac{1}{2}\frac{\left|\varepsilon_{\mathrm{p},33}^{\mathrm{T}} - \varepsilon_{\mathrm{p},33}^{\mathrm{B}}\right|}{\max\left\{\left|\varepsilon_{\mathrm{p},33}^{\mathrm{T}}\right|, \left|\varepsilon_{\mathrm{p},33}^{\mathrm{B}}\right|\right\}} \quad \text{where} \quad \Omega \in [0,1] \tag{7}$$

where $\varepsilon_{\mathrm{p},33}^{\mathrm{T}}$ and $\varepsilon_{\mathrm{p},33}^{\mathrm{B}}$ are the through-thickness plastic strain at the top and bottom integration points of the shell element, respectively. The Cockcroft-Latham failure parameter $W_{\mathrm{c}}$ is then found by linear interpolation between the failure parameter in pure membrane ($\Omega = 0$, $W_{\mathrm{c}} = W_{\mathrm{c}}^{\mathrm{m}}$) and pure bending ($\Omega = 1$, $W_{\mathrm{c}} = W_{\mathrm{c}}^{\mathrm{b}}$), viz.

$$W_{\mathrm{c}} = \Omega W_{\mathrm{c}}^{\mathrm{b}} + (1-\Omega) W_{\mathrm{c}}^{\mathrm{m}} \tag{8}$$

The effect of the bending parameter on the failure locus in plane stress is given in Figure 10 below.

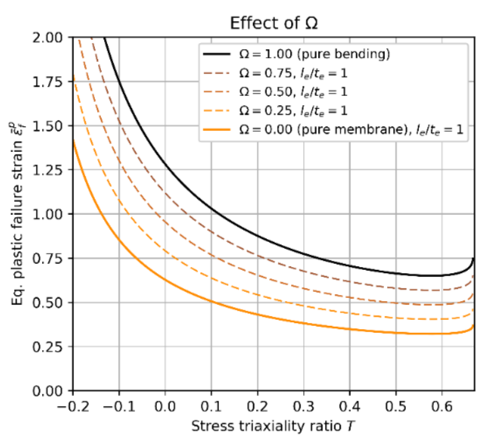


Figure 10: Effect of bending parameter *Ω* on the failure locus.

As there is no localization in pure bending, only the Cockcroft-Latham failure parameter in membrane is regularized, i.e.

$$W_{\mathrm{c}}^{\mathrm{m}} = W_{\mathrm{c}}^{\mathrm{l}} + \left(W_{\mathrm{c}}^{s} - W_{\mathrm{c}}^{\mathrm{l}}\right) \exp\left[-c\left(\frac{l_{\mathrm{e}}}{t_{\mathrm{e}}} - 1\right)\right] \tag{9}$$

where $W_{\mathrm{c}}^{\mathrm{l}}$ is the horizontal asymptote as the length-to-thickness ratio $l_{\mathrm{e}}/t_{\mathrm{e}} \rightarrow \infty$, $W_{\mathrm{c}}^{s}$ is the value for $l_{\mathrm{e}}/t_{\mathrm{e}} = 1$, and $c$ is a parameter controlling the slope.

## 3.1 GISSMO

To obtain the Hershey-Hosford equivalent stress (Equation (2)) as in the simulation with *MAT_258 (see Section 3.1) *MAT_ADD_EROSION is combined with *MAT_036/*MAT_3-PARAMETER_BARLAT. Isotropic material behavior is achieved by setting $R_{00} = R_{45} = R_{90} = 1.0$. The work hardening is prescribed through a load curve, where a discretized Voce work hardening is tabulated based on Equation (3).

Damage coupling is used, viz.

$$\boldsymbol{\sigma} = \left(1 - \widetilde{D}\right)\widetilde{\boldsymbol{\sigma}} \tag{10}$$

where $\boldsymbol{\sigma}$ is the effective Cauchy stress tensor, $\widetilde{\boldsymbol{\sigma}}$ is the Cauchy stress tensor, and $\widetilde{D}$ is the damage variable defined as

$$\widetilde{D} = \begin{cases} 0 & \text{if } F < 1 \\ \left(\dfrac{D - D_{\mathrm{crit}}}{1 - D_{\mathrm{crit}}}\right)^{\mathrm{FADEXP}} & \text{if } F = 1 \end{cases} \tag{11}$$

Here FADEXP is a parameter controlling how fast the damage grows. The damage evolution is defined as

$$\dot{D} = \frac{\mathrm{DMGEXP} \cdot D^{\left(1 - \frac{1}{\mathrm{DMGEXP}}\right)}}{\mathrm{LCREGD} \cdot \varepsilon_{\mathrm{f}}(\eta)} \tag{12}$$

Where DMGEXP is a damage growth parameter, LCREGD is the tabulated regularization curve and $\varepsilon_{\mathrm{f}}(\eta)$ is the fracture locus tabulated as a function of the stress triaxiality $\eta$, and $D_{\mathrm{crit}}$ is the value of $D$ when a localized neck develops ($F = 1$). The instability parameter, $F$, evolves according to

$$\dot{F} = \frac{\mathrm{DMGEXP} \cdot F^{\left(1 - \frac{1}{\mathrm{DMGEXP}}\right)}}{\varepsilon_{\mathrm{crit}}(\eta)} \dot{p} \tag{13}$$

where $\varepsilon_{\mathrm{crit}}(\eta)$ is the tabulated instability locus defining the point of localized necking.

# 4 Calibration

Both failure models were run with identical work hardening parameters. LS-OPT® was used in an inverse modelling approach to obtain the work hardening parameters from a UT200 uniaxial tension test (see Section 2.1) simulated in LS-DYNA R9.3 using solid elements. The solid element model used had three symmetry planes, with 4 elements (ELFORM=1) over the thickness, see Figure 11.

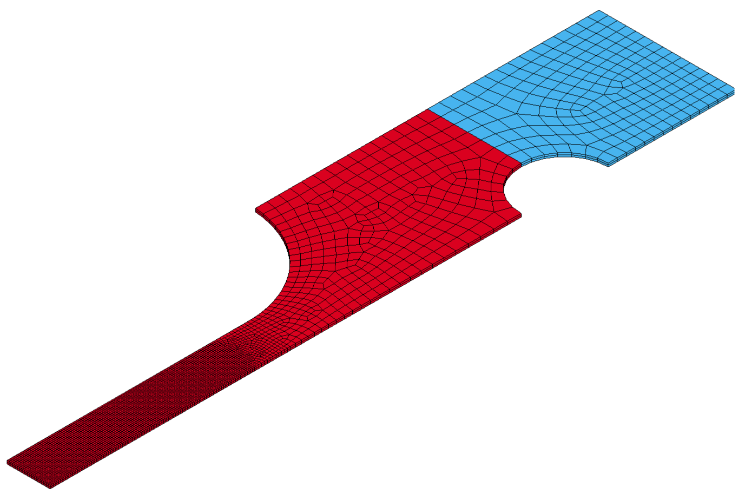

Figure 11: Finite element model used in the inverse modelling approach.

To obtain the Hershey-Hosford equivalent stress with $a = 6$ (see Figure 9), *MAT_033 was used. Anisotropy was turned off by setting $A = B = C = D = F = G = H = 1$. The material constants and the hardening parameters are given in Table 1.

Table 1: Material constants and work hardening parameters for Docol 1400M

| Material constants | | | | Work hardening parameters | | | | | | |
|---|---|---|---|---|---|---|---|---|---|---|
| $\rho$ $(\mathrm{kg/m^3})$ | $E$ (GPa) | $\nu$ $(-)$ | $a$ $(-)$ | $\sigma_0$ (GPa) | $Q_1$ (GPa) | $\theta_1$ (GPa) | $Q_2$ (GPa) | $\theta_2$ (GPa) | $Q_3$ (GPa) | $\theta_3$ (GPa) |
| 7850 | 210.0 | 0.33 | 6.0 | 1.2 | 0.25 | 196.6 | 0.097 | 13.01 | 0.2 | 1.2 |

A comparison between simulation and experiment is given in Figure 12.

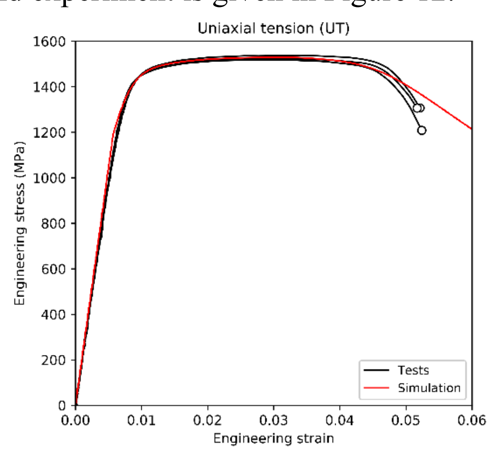


Figure 12: Solid element simulation vs. experiment for uniaxial tension.

## 4.1 *MAT_258

Calibration of the failure model in *MAT_258 is straightforward. Since we are only using the standard Cockcroft-Latham criterion ($\gamma = \phi = 1$ in Equation (6)) we only need one uniaxial tension test to fully calibrate the failure locus together with the regularization expression.

First, we do a simulation of the uniaxial tension test using solid elements. The major principal stress, $\sigma_1$, and the equivalent plastic strain, $p$, is then extracted from the centermost element inside the neck. These two quantities are then used to calculate the critical Cockcroft-Latham parameter in bending, viz.

$$W_{\mathrm{c}}^{\mathrm{b}} = \int_0^{p_{\mathrm{f}}} \sigma_1 \mathrm{d}p \tag{14}$$

where $p_{\mathrm{f}}$ is the equivalent plastic strain at failure. Now the Cockcroft-Latham failure parameters associated with membrane loading needs to be determined, this is accomplished by running several single shell elements in uniaxial tension, where the applied displacement history is taken from virtual extensometers extracted from the solid element simulation, see Figure 13.

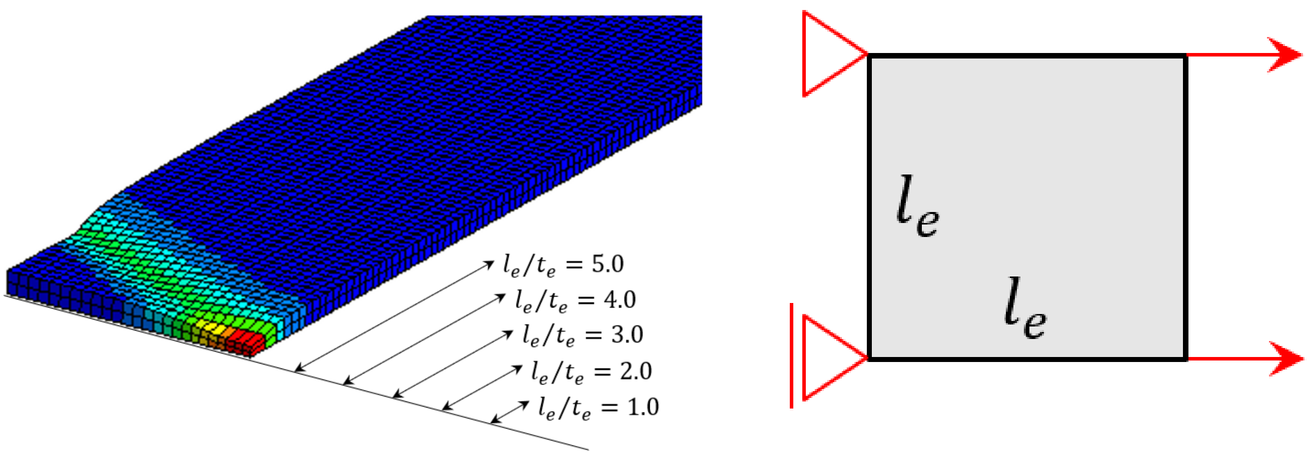


(a) (b)

Figure 13: (a) virtual extensometers from solid element simulation, and (b) single shell element in uniaxial tension.

From the 5 single shell element simulations, we obtain 5 critical Cockcroft-Latham parameters for membrane deformation, viz.

$$W_{\mathrm{c},i}^{\mathrm{m}} = W_{\mathrm{c}}^{\mathrm{m}}(l_{\mathrm{e}}/t_{\mathrm{e}} = i) = \int_0^{p_{\mathrm{f}}} \sigma_1 \mathrm{d}p \quad \text{for } i = \{1,2,3,4,5\} \tag{15}$$

These five parameters are then used to find the three parameters associated with the regularization curve (Equation (9)) as shown in Figure 14.

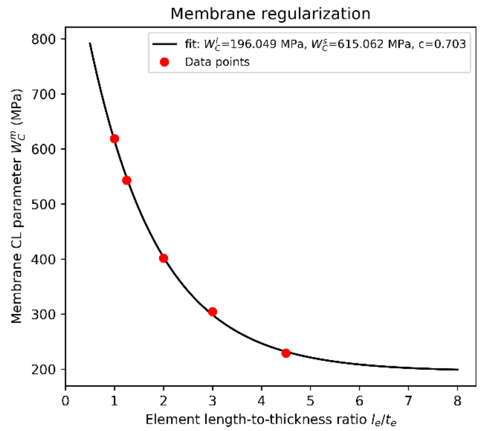


Figure 14: Regularization curve.

The parameters obtained for the failure model in *MAT_258 are given in Table 2.

Table 2: Failure parameters for *MAT_258.

| $W_c^b$ (MPa) | $W_c^l$ (MPa) | $W_c^s$ (MPa) | $c$ | $\phi$ | $\gamma$ |
|---|---|---|---|---|---|
| 1276.60 | 196.05 | 615.06 | 0.703 | 1.0 | 1.0 |

## 4.2 GISSMO / *MAT_ADD_EROSION

To calibrate failure with GISSMO, all the experimental tests given in Section 2 was used, i.e. UT, PST, ISS and NK. A tabulated failure locus ($\varepsilon_f(\eta)$) together with a tabulated instability locus ($\varepsilon_{crit}(\eta)$) was used. The stress triaxiality for each point was kept constant, while the magnitude of the equivalent plastic failure strain and the necking strain, together with DMGEXP and FADEXP were optimized using LS-OPT, see Figure 15.

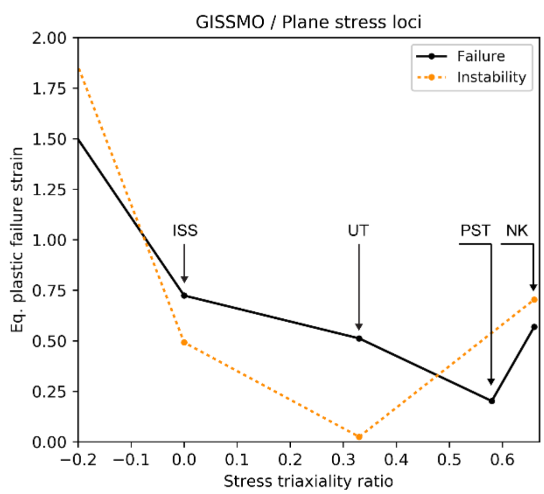


Figure 15: Optimized failure and instability loci using GISSMO.

The regularization curve LCREGD was found by running UT simulations with different element sizes, see Figure 16.

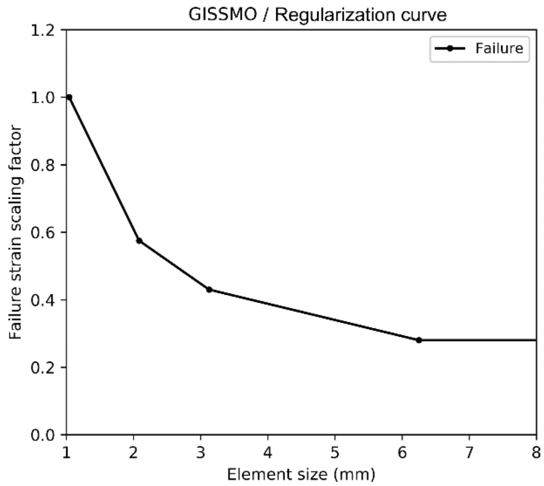


| Element size (mm) | Failure strain scaling factor |
|---|---|
| 0.000 | 1.500 |
| 1.042 | 1.000 |
| 2.083 | 0.575 |
| 3.125 | 0.430 |
| 6.250 | 0.280 |
| ∞ | 0.280 |

Figure 16: Regularization curve (LCREGD) for the GISSMO failure model.

All parameters obtained from the optimization procedure in LS-OPT are given in Table 3.

Table 3: Tabulated failure and fracture loci and parameters for GISSMO failure model

| $\eta$ | $\varepsilon_{\mathrm{f}}$ | $\varepsilon_{\mathrm{crit}}$ |
|---|---|---|
| -0.66 | 5.000 | 5.000 |
| -0.33 | 2.000 | - |
| 0.00 | 0.724 | 0.492 |
| 0.33 | 0.512 | 0.025 |
| 0.58 | 0.202 | - |
| 0.67 | 0.569 | 0.704 |

| DMGEXP | FADEXP |
|---|---|
| 4.76672 | 1.31546 |

## 5 Benchmark tests

Three benchmark tests were performed in the Zwick/Roell BUP 600 testing machine: S20, S100 and S150, where the number denotes the width of the bridge, see Figure 17. The geometries were chosen to obtain three different stress states, i.e. S20 is close to uniaxial tension, S100 is biaxial tension, and S150 (full circle) is equibiaxial tension. The same experimental set-up as described in Section 2.4 was used for all tests, and two repetitions were performed per geometry.

Each test was simulated in LS-DYNA using both *MAT_258 and GISSMO. Additionally, three different element sizes were used: $l_e/t_e \approx \{1,2,3\}$.

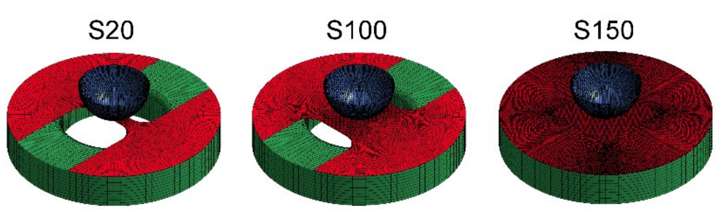


Figure 17 Finite element models used in the benchmark simulations.

As seen from Figures 18(a) and 18(b) there is good agreement between simulation and experiment using both failure models. It is also evident that the effect of element size is small, meaning that the regularization procedure in both models works well. In terms of the point of fracture GISSMO performs slightly better than *MAT_258.

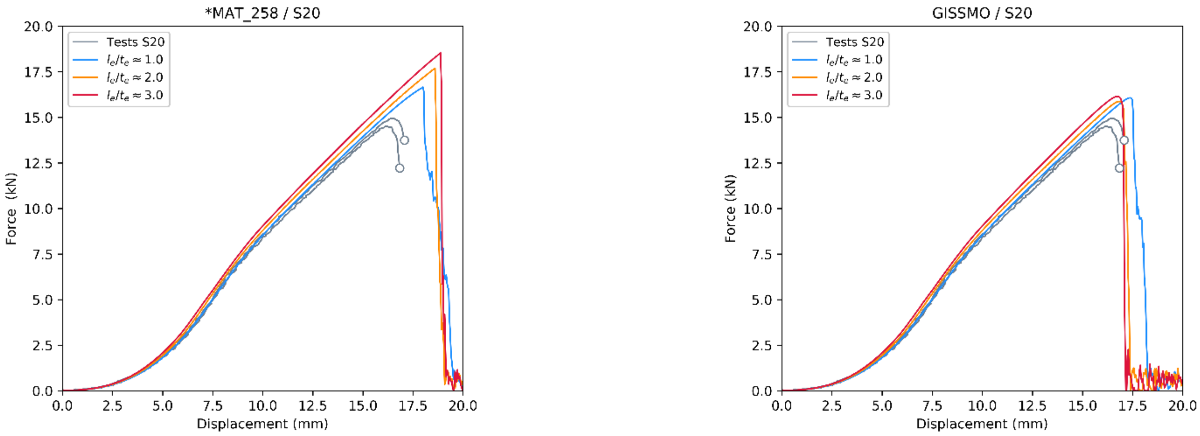


(a) (b)

Figure 18: Simulation vs. experiment for the S20 specimens using (a) *MAT_258 and (b) GISSMO.

For the S100 experiments, *MAT_258 and GISSMO yields close to identical results as shown in Figures 19(a) and 19(b). Failure prediction in both simulation models is within the scatter from experiments, and the regularization procedure behaves as it should.

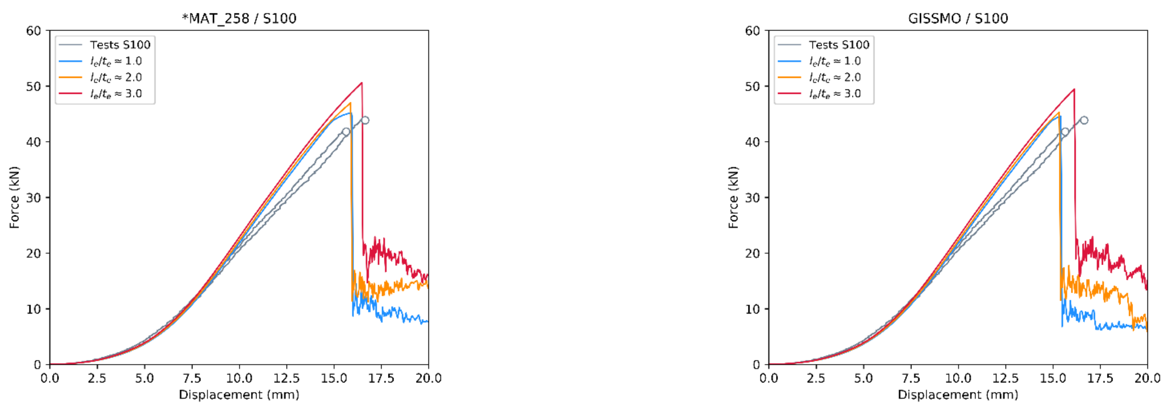


(a) (b)

Figure 19: Simulation vs. experiment for the S100 specimens using (a) *MAT_258 and (b) GISSMO.

For the equibiaxial S150 experiments, there is a quite large difference between *MAT_258 and GISSMO, see Figure 20. GISSMO predicts that failure occurs too late, while *MAT_258 predicts that failure occurs to early. The regularization in *MAT_258 is not effective enough, since a clear effect of the element size can be seen on failure prediction in Figure 20(a).

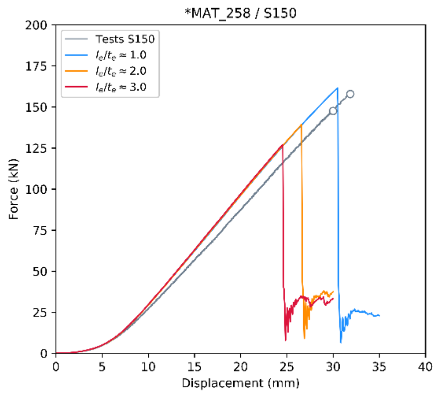


(a)

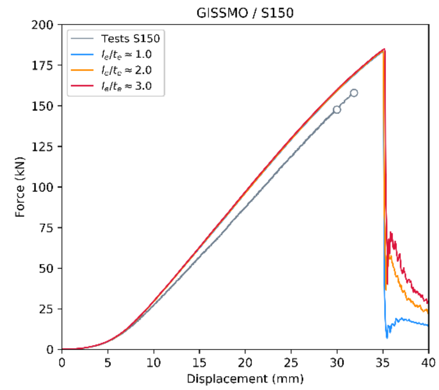


(b)

Figure 20 Simulation vs. experiment for the S150 specimens using (a) *MAT_258 and (b) GISSMO.

This is due to a combination of membrane loading and improper discretization of the geometry with the largest elements, further increasing the contribution of membrane loading in the failure assesment, which in turns reduces the failure strain21, meaning that the reason for too early failure prediction is mainly due to the mesh and the type of test, rather than the regularization procedure not working as it should. Not also that

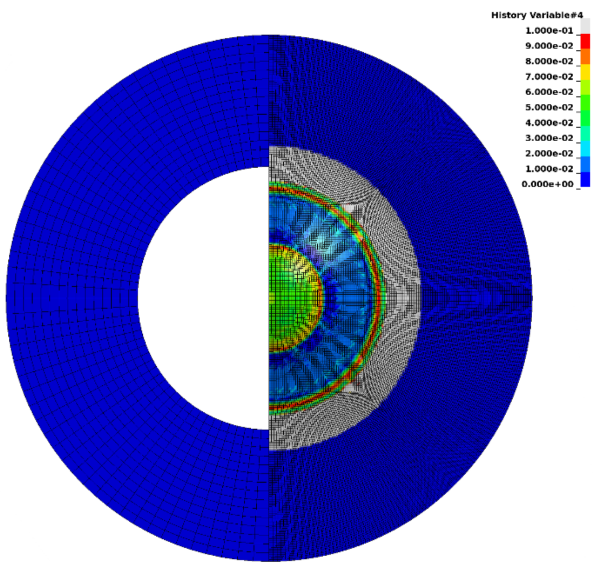


(a)

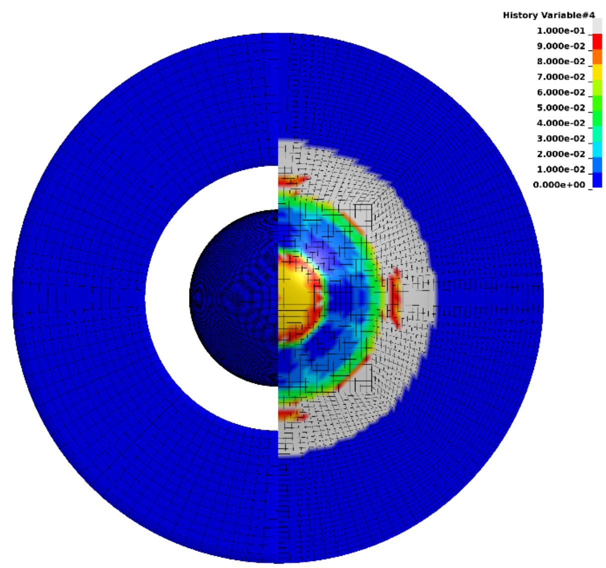


(b)

Figure 21: Comparison of the bending parameter for the S150 simulations with (a) le/te=1 and (b) le/te=3.

## 6 Validation

Validation experiments were performed on cold-formed hat profiles (Figure 22), the support plate was made of Docol 600DL and was fastened with pop-rivets. The profiles were subjected to three-point bending, where the punch had a constant crosshead velocity of 10 mm/min. A trigger was added directly beneath the punch to ensure that the profiles failed at the same position in each of the four repetitions. To reduce friction, grease was added between the punch and the hat profile, as well as between the supports and the hat profile.

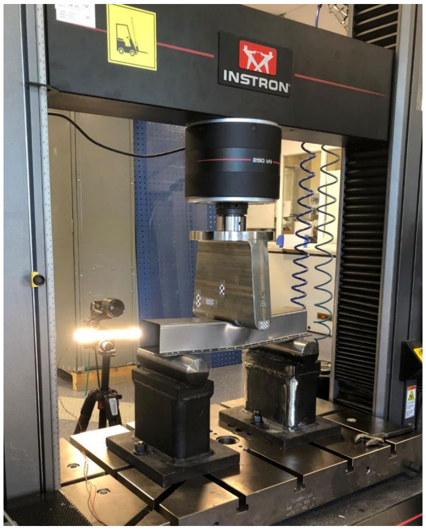


(a)

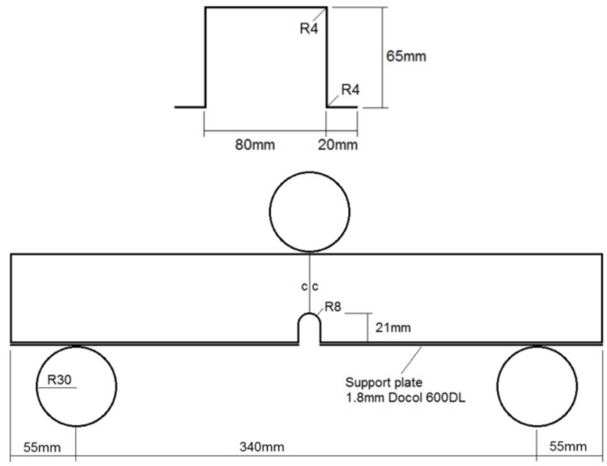


(b)

Figure 22: The experimental set-up (a) and the specimen geometry (b).

Three different mesh sizes were used for the simulation models, $l_e/t_e = \{1,2,3\}$. ELFORM = 2 was used, with 5 integration points over the thickness of the shell element. The automatic single surface contact algorithm was used with SOFT=1 and FS=FD=0.1, i.e. a constant friction coefficient. The FE model is shown in Figure 23. To simplify the modelling approach the pop-rivets were not included, meaning that the support plate and the hat profile was assumed to be fully bonded together.

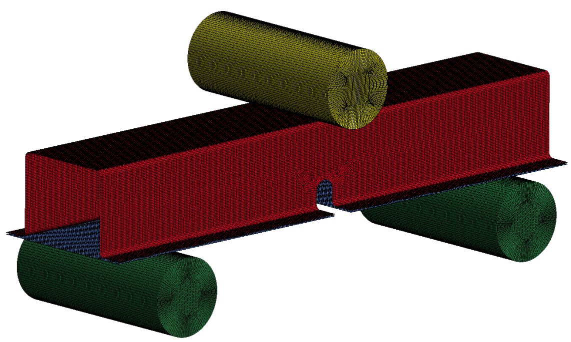

Figure 23: Finite element model of the validation test.

A comparison between simulations with *MAT_258 and experiments is shown in Figure 24(a), while the simulations with GISSMO are shown in Figure 24(b). In both cases the agreement with experiments are excellent. It is also evident that the regularization procedure handles the different mesh sizes well. Furthermore, considering the simplicity of the *MAT_258 model, the model predictions are excellent.

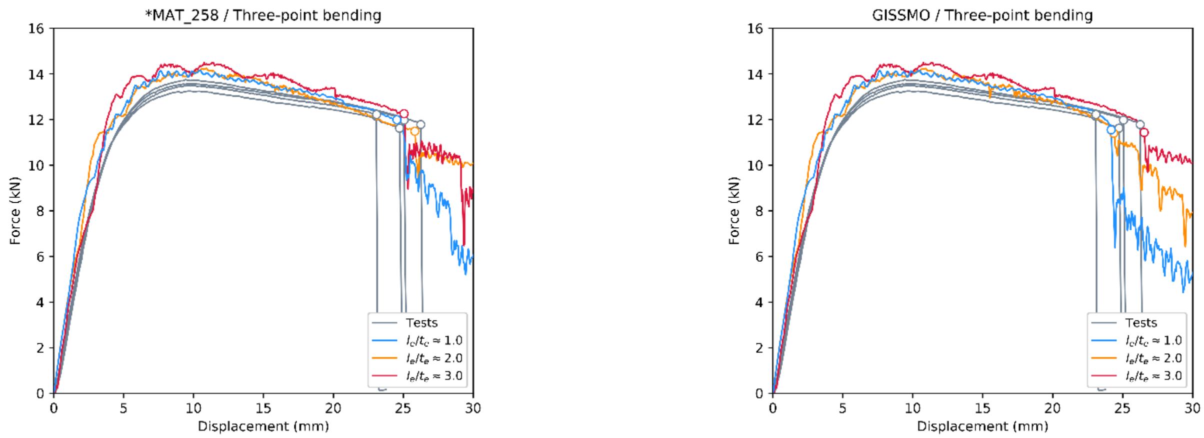


(a) (b)

Figure 24 Simulation vs. experiments for the validation experiments using (a) *MAT_258 and (b) GISSMO.

Figure 25 shows a comparison between the component after failure from experiment and simulation.

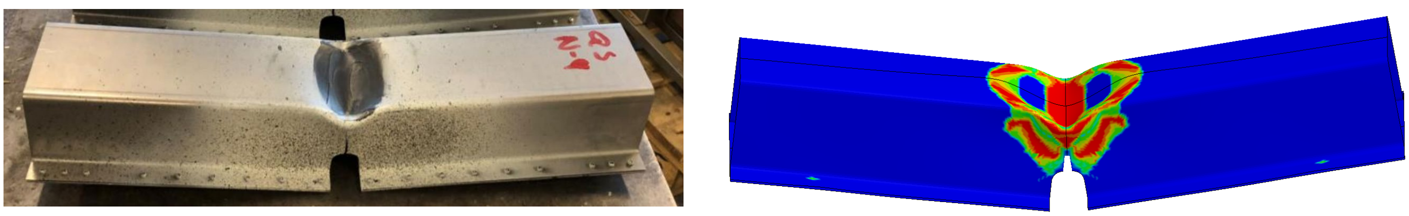

(a) (b)

Figure 25 Comparison of components after failure in (a) simulations and (b) experiments with the bending parameter indicated.

## 7 Concluding remarks

In this study we calibrate and compare two failure models for shells in LS-DYNA: the relatively new *MAT_258 and GISSMO. *MAT_258 requires only one uniaxial tension test to calibrate if choosing the simplest failure criterion, i.e. the Cockcroft-Latham [8] failure criterion. On the other hand, there is no limitation in the number of tests that can be used to calibrate GISSMO given its tabulated nature, meaning that GISSMO is an extremely flexible failure criterion that in most cases will yield very good results, but at the cost of requiring many calibration experiments.

Both failure models have been applied to 3 benchmark tests in a Zwick/Roell BUP 600 testing machine, and one three-point bending test of a purpose-made hat profile. All in all, both failure models give excellent results. In terms of computational time *MAT_258 slightly outperforms GISSMO, but it should be noted that this is not caused by GISSMO, but rather by the material model that was chosen to obtain the Hershey-Hosford yield surface (*MAT_036).

## References


[1] Andrade, F. X. C., Feucht, M., Haufe, A., Neukamm, F. *An incremental stress state dependent damage model for ductile failure prediction*. International Journal of Fracture, 200(1–2), 127–150, 2016.

[2] Costas, M., Morin, D., Hopperstad, O. S., Børvik, T., Langseth, M. *A through-thickness damage regularisation scheme for shell elements subjected to severe bending and membrane deformations*. Journal of the Mechanics and Physics of Solids, 123, 190–206, 2019. https://doi.org/10.1016/j.jmps.2018.08.002

[3] Gruben, G., Langseth, M., Fagerholt, E., Hopperstad, O. S. *Low-velocity impact on high-strength steel sheets: An experimental and numerical study*. International Journal of Impact Engineering, 88, 153–171, 2016. https://doi.org/10.1016/j.ijimpeng.2015.10.001

[4] Gruben, G., Morin, D., Langseth, M., Hopperstad, O. S. *Strain localization and ductile fracture in advanced high-strength steel sheets*. European Journal of Mechanics, A/Solids, 61, 315–329, 2017. https://doi.org/10.1016/j.euromechsol.2016.09.014

[5] Gruben, G., Hopperstad, O. S., Borvik, T. (2012). *Evaluation of uncoupled ductile fracture criteria for the dual-phase steel Docol 600DL*. International Journal of Mechanical Sciences, 62(1), 133–146. https://doi.org/10.1016/j.ijmecsci.2012.06.009

[6] Costas, M., Morin, D., Hopperstad, O. S., Børvik, T., Langseth, M. (2020). *Corrigendum to "A through-thickness damage regularisation scheme for shell elements subjected to severe bending and membrane deformations"*. Journal of the Mechanics and Physics of Solids, 135, 103794. https://doi.org/10.1016/j.jmps.2019.103794

[7] Nakajima K., Kikuma, T. Hasuka, K. (1968). *Study on the formability of steel sheets.* Report 8517-8530

[8] Cockcroft, M. G., Latham, D. J. (1968). *Ductility and workability of metals.* Journal of the Institute of Metals, 96, 33–39.